Visualizing and Understanding Ordered Surface Phases during the Ullmann Coupling Reaction

Tedros A. Balema[a], Jiayuan Miao[a], Natalie A. Wasio[a], Colin J. Murphy[a], Amanda M. Larson[a], Dipna A. Patel[a], Yu-Shan Lin[a]* and E. Charles H. Sykes[a]*

[a]*Department of Chemistry, Tufts University, Medford MA 02155*

* Email: charles.sykes@tufts.edu and yu-shan.lin@tufts.edu

Abstract

The more than century old copper metal catalyzed Ullmann coupling reaction of aryl halides has seen renewed interest from the nanoscience community as a means to perform on-surface C–C coupling based self-assembly of extended 2D structures. Furthermore, recent experiments have revealed that Ullmann coupling is not a direct process, rather it proceeds *via* an organometallic intermediate comprised of a removed Cu surface atom that coordinates two phenyl groups. We have undertaken a low-temperature scanning tunneling microscopy study to investigate the interaction and ordering of the surface-bound reactants, organometallic intermediates, and products and found that these species all self-assemble into dense 2D islands that mimic the high surface coverages expected during typical Ullmann coupling reaction conditions. By comparing and contrasting a series of substituted bromobenzene reactants we found that the 2D packing density and structure depend strongly on the functionality of the substituents. Furthermore, our calculations of the charge distribution in the intermediates and products explain the observed packing structures of the highly ordered 2D phases. This study provides atomic-scale snapshots of the catalytic surface of this important reaction and can guide further model studies of the molecular scale mechanism of the Ullmann coupling reaction.

1. Introduction

The Ullmann coupling reaction is a classic metal-catalyzed synthetic method for forming C−C bonds where two aryl halides are coupled over a copper catalyst to form a biaryl molecule.[1,2] The original Ullmann reaction traditionally required stoichiometric amounts of copper and aryl halides in order to proceed. However, modern iterations of the reaction have found that catalytic amounts of copper bound ligands and a wide range of copper species can be used to promote the reaction.[3–23] Unlike other metal-mediated reactions, the Ullmann mechanism is not as fully understood despite its widespread study and application. This is due its unpredictable selectivity coupled with its sensitivity to functional groups and the need for extreme reaction conditions.[24–28]

Through the use of surface techniques, such as scanning tunneling electron microscopy (STM), the formation and surface diffusion of Ullmann coupling intermediates have been studied by tracking the reaction from the starting aryl reagents, through the intermediates and the final biaryl products and this mechanism is summarized schematically in **Figure 1**.[29–42] On a Cu(111) surface, Ullmann coupling intermediates do spontaneously self-assemble into 2D crystals and these assemblies have demonstrated interesting properties ranging from a diversity of domain types to molecular scale machines.[43–48] Due to current limitations in 2D crystal engineering, it is not yet possible to *a priori* predict the relationships between the molecular structure of the aryl halide precursor and the crystal packing of the intermediate and final biaryl product; oftentimes slight changes in the starting reagent result in a huge impact on the packing structures of the intermediate and product. One of the key features of the Ullmann coupling reaction on a copper surface is that in the intermediate stage the aryls to be coupled are bonded to a copper atom that is removed from the surface (**Figure 1**, middle panel).[37,42,49,50] Compared to the biaryl product, the intermediates are slightly larger and pack quite differently as this manuscript will show.

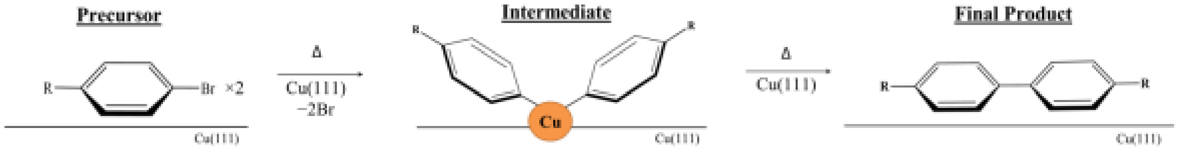

Figure 1: Schematic of the Ullmann coupling reaction of an aryl halide on Cu(111).

In this study, four different Ullmann coupling reactions are compared through their respective intermediates and products (**Table 1**). Such a comparative study has not yet been done and should serve as a guide in predicting Ullmann coupling formation behaviors. 1-Bromo-4-ethylbenzene is used as a control due to how extensive the intermediates have been studied in the past; they behave as altitudinal rotors and lack other features beyond the ethyl-tail.[45] By simply adding a fluorine atom on the *ortho* position with respect to the ethyl tail or changing the ethyl tail itself to a 1,1,1-trifluoroethyl group or a methoxy, these three reactants all yield quite distinct structures as one follows the various stages of the Ullmann coupling reaction. In this manuscript, the Ullmann intermediates and products for comparison are listed below in **Table 1**, for brevity each of their names have been assigned to either an **I_x** or **P_x** label.

Table 1: Structures of the Ullmann coupling intermediates and products for comparison, each intermediate or product has been assigned to an **I_x** or a **P_x** name, respectively.

Reactant Structure	Intermediate Structure	Assigned Intermediate Name	Product Structure	Assigned Compound Name
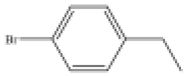	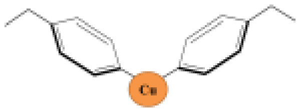	**I_1**	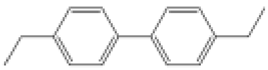	**P_1**
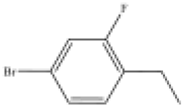	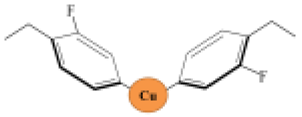	**I_2**	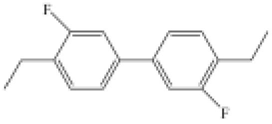	**P_2**
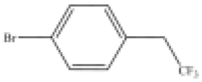	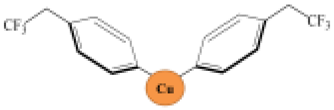	**I_3**	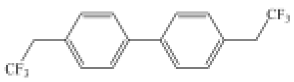	**P_3**
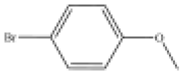	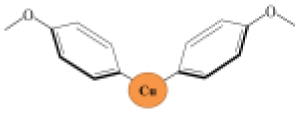	**I_4**	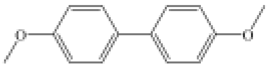	**P_4**

2. Experimental Methods

All low-temperature STM (LT-STM) experiments were performed in an Omicron Nanotechnology GmbH low-temperature microscope, operating under a base pressure of $<1 \times 10^{-11}$ mbar. The MaTecK Cu(111) single crystal was cleaned with multiple cycles of Ar+ sputtering and 1000 K annealing. Prior to deposition of molecules the cleanliness of the crystal was determined by STM. Etched W tips were used to record all STM images. 1-Bromo-4-ethylbenzene (99.9%), 4-bromo-1-ethyl-2-fluorobenzene (>95%) and 1-bromo-4-methoxybenzene (99%) were degassed by multiple freeze/pump/thaw cycles. 1-bromo-4-(2,2,2-trifluoroethyl)benzene (97%) was a solid thus it did not need to undergo freeze/pump/thaw cycles . The precursor molecules were vapor deposited on to a Cu(111) sample held at 5 K through a collimated molecular doser attached to a precision leak valve. Anneals from 5 K were performed in order to equilibrate the deposited molecular ensembles and to induce reaction by removing the sample from the cryogenically cooled stage of the STM and placing it into a sample holder held at room temperature in the UHV chamber for a predetermined length of time. All anneals above 300 K were performed using a resistively heated sample stage. The crystal was then cooled back to 5 K by putting it back into the STM stage for imaging.

3. Calculation Methods

The calculations were performed with the B3LYP functional and the 6-311+G(d,p) basis set using the Gaussian 09 Software,[51] with integration grid set to "ultrafine". The gas-phase energies of the four reactants with Br replaced by H, $\mathbf{R_1}$, $\mathbf{R_2}$, $\mathbf{R_3}$, $\mathbf{R_4}$ (**Table S1**) were scanned with a step size of 1° rotating around the C sp^3–C sp^2 bond (for $\mathbf{R_1}$, $\mathbf{R_2}$ and $\mathbf{R_3}$) or O–C sp^2 bond (for $\mathbf{R_4}$). The gas-phase energies of the products $\mathbf{P_1}$, $\mathbf{P_2}$, $\mathbf{P_3}$, $\mathbf{P_4}$ (**Table 1**) were scanned with a step size of 30° rotating around the two C sp^3–C sp^2 bonds for $\mathbf{P_1}$, $\mathbf{P_2}$, $\mathbf{P_3}$ or around the two O–C sp^2 bonds for $\mathbf{P_4}$ (dihedrals d_1 and d_3, defined in **Table S3** and **Table S5**) and the C sp^2–C sp^2 bond connecting the two benzene rings (dihedral d_2, defined in **Table S3** and **Table S5**). The conformations at potential energy minima were used as the initial structures for further optimization. Because of the interaction between the product molecules and the Cu surface, the biphenyl ring likely lies flat on the surface. Therefore, we also performed calculations where we fixed d_2 in the conformation where the two benzene rings lie on the same plane. The dipoles and quadrupoles of the optimized molecules were derived using the partial charges calculated according to the Merz-Singh-Kollman scheme.[52]

4. Results and Discussion

The progression of each Ullmann coupling reaction was tracked from the intact precursor molecules, through the intermediates ($\mathbf{I_x}$), to the biphenyl products ($\mathbf{P_x}$) as seen in **Figures 2** and **3**. In **Figure 2** the conversion of 1-bromo-4-ethylbenzene → $\mathbf{I_1}$ → $\mathbf{P_1}$ and 4-bromo-1-ethyl-2-fluorobenzene → $\mathbf{I_2}$ → $\mathbf{P_2}$ were tracked. Upon deposition onto the Cu sample held at 5 K and annealing to 80 K, the intact 1-bromo-4-ethylbenzene molecules cluster in small groups of six molecules (**Figure 2A***I*). Annealing the sample to 220 K leads to C–Br bond cleavage and formation of the organometallic intermediate structure $\mathbf{I_1}$, followed by cooling to 5 K for imaging the structures (**Figure 2A***II*). Further annealing the sample to 346 K yields the final product $\mathbf{P_1}$ (**Figure 2A***III*). In the case of 4-bromo-1-ethyl-2-fluorobenzene, dosing onto the Cu sample held at 5 K and annealing to 80 K yields larger disordered structures of the intact molecule (**Figure 2B***I*). Annealing the sample to 220 K yields the organometallic intermediate structure $\mathbf{I_2}$, followed by cooling to 5 K for imaging (**Figure 2B***II*). Further annealing the sample to 380 K yields the final product $\mathbf{P_2}$ (**Figure 2B***III*).

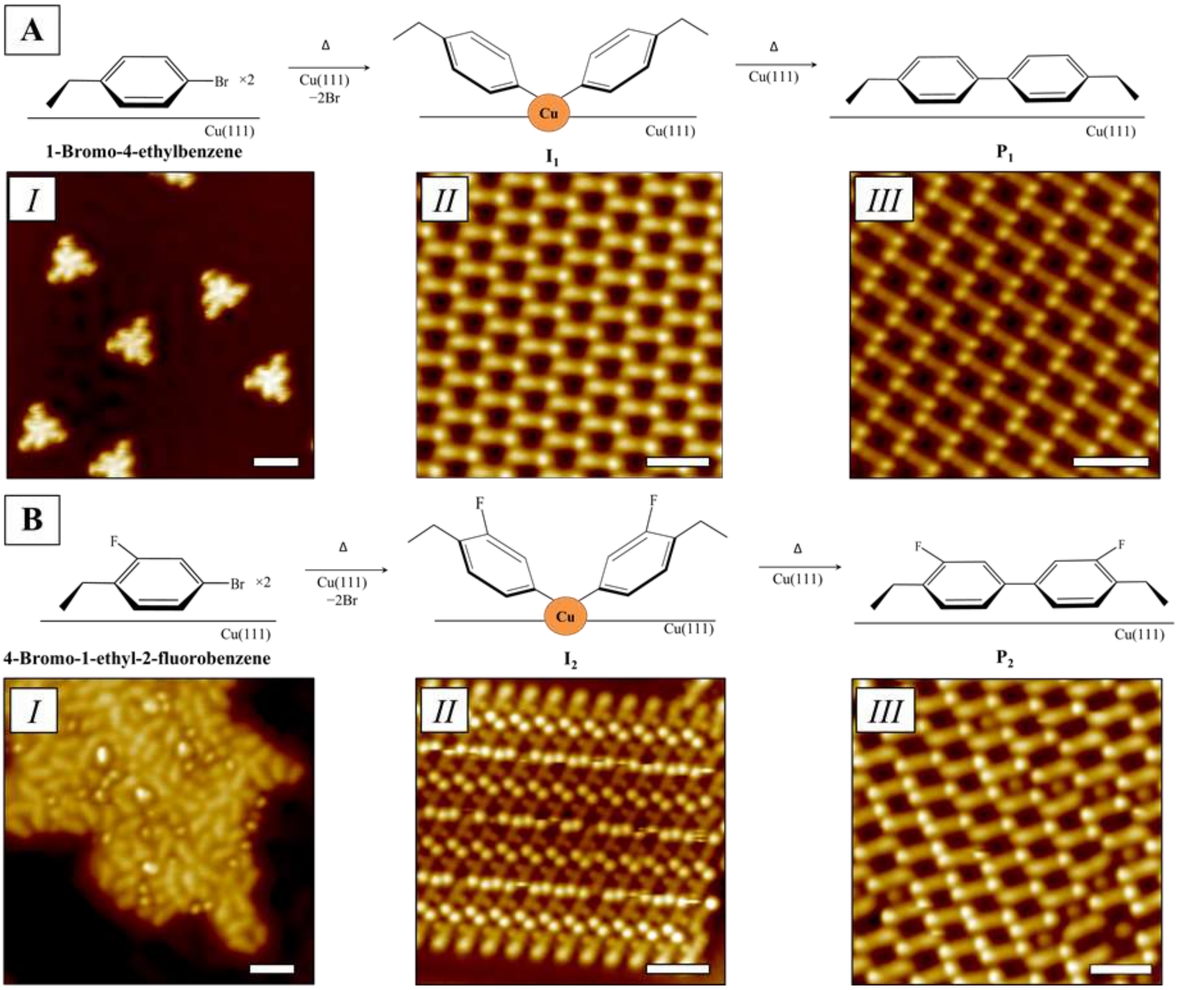

Figure 2: Schematics and accompanying STM images of the Ullmann coupling reaction of various aryl halides on Cu(111). **A**. 1-Bromo-4-ethylbenzene → $\mathbf{I_1}$ → $\mathbf{P_1}$. **B**. 4-Bromo-1-ethyl-2-fluorobenzene → $\mathbf{I_2}$ → $\mathbf{P_2}$. Imaging Conditions: **A**. *I*. 50 mV, 10 pA; *II*. −10 mV, 10 pA; *III*. −10 mV, 50 pA. **B**. *I*. 50 mV 10 pA; *II*. 10 mV 100 pA; *III*. 10 mV, 100 pA. Scale bars: 2 nm.

In **Figure 3**, the conversion of 1-bromo-4-(2,2,2-trifluoroethyl)benzene to 1-ethyl-4-(4-ethyl-3-fluorophenyl)-2-fluorobenzene and 1-bromo-4-methoxybenzene to 4,4'-dimethoxybiphenyl were tracked. Since 1-bromo-4-(2,2,2-trifluoroethyl)benzene is a solid and required deposition in the preparation chamber on the room temperature, sample imaging the intact precursor molecules was not possible. Annealing the sample to 220 K forms the intermediate structure $\mathbf{I_3}$ followed by further cooling to 80 K for imaging (**Figure 3A***I*). Further annealing the sample to 400 K yields the final product $\mathbf{P_3}$ (**Figure 3A***II*). When 1-bromo-4-methoxybenzene was deposited upon the Cu sample and annealed to 120 K, the formation of long range ordered arrays consisting of a trio of molecules were observed (**Figure 3B***I*). Annealing the sample to 220 K formed the intermediate structure $\mathbf{I_4}$, followed by further cooling to 5 K for imaging (**Figure 3B***II*). Annealing the sample further to 400 K yields the final product $\mathbf{P_4}$ (**Figure 3B***III*).

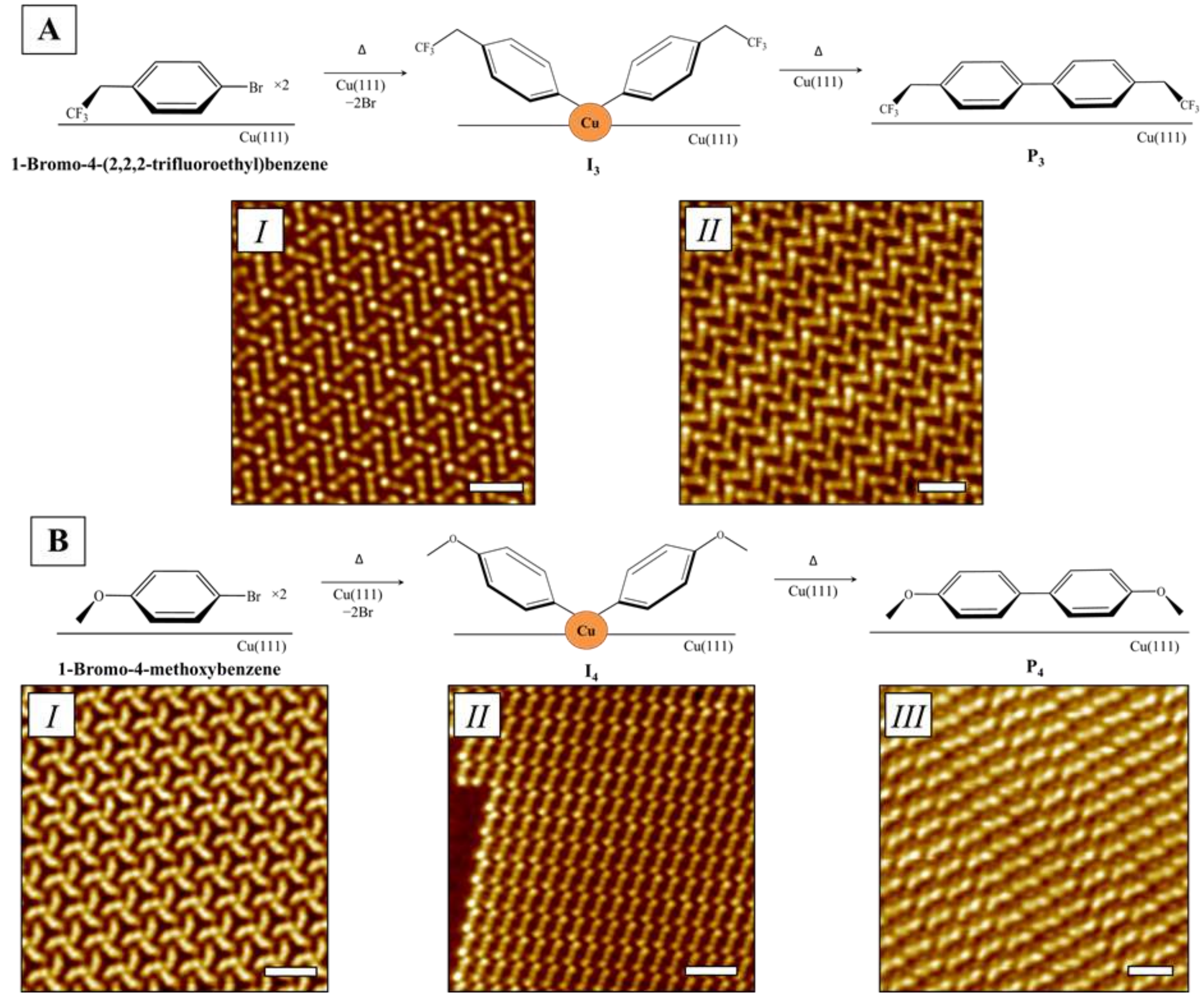

Figure 3: Schematics and accompanying STM images of the Ullmann coupling reaction of various aryl halides on Cu(111). **A**. 1-Bromo-4-(2,2,2-trifluoroethyl)benzene → **I**$_3$ → **P**$_3$. **B**. 1-Bromo-4-methoxybenzene → **I**$_4$ → **P**$_4$. Imaging Conditions: **A**. *I*. 100 mV 50 pA; *II*. 200 mV, 200 pA. **B**. *I*. 50 mV, 100 pA; *II*. 100 mV, 50 pA; *III*. 200 mV, 200 pA. Scale bars: 2 nm.

Comparing the organometallic intermediates of the four Ullmann coupling reactions observed, it is noticeable that they all form highly ordered arrays, as shown in **Figure 4**. In **Figure 4A**, it is observed that **I**$_1$ has a parallelogram unit cell with dimensions of $3\sqrt{3} \times \sqrt{19}$. It has an open brick wall motif. It can be seen in **Figure 4B** that although **I**$_2$ has an almost identical molecular structure to **I**$_1$ (only differing in having a fluorine in the *ortho* position with respect to the ethyl tail), the structure of the intermediate overlayer is very different. Its unit cell is a $4 \times 2\sqrt{31}$ parallelogram which is significantly larger and differently arranged compared to **I**$_1$. **Figure 4C** shows that **I**$_3$ has a rectangular unit cell with dimensions of $4\sqrt{3} \times 7$. The very different manner in how the molecules are orientated (**Figure 4C**) appears to imply significant electrostatic interactions, which makes sense considering the presence of highly polar $-CH_2CF_3$ tails. In the case of **I**$_4$ in **Figures 4D**, a rectangular unit cell structure was observed with $4 \times 3\sqrt{3}$ dimensions.

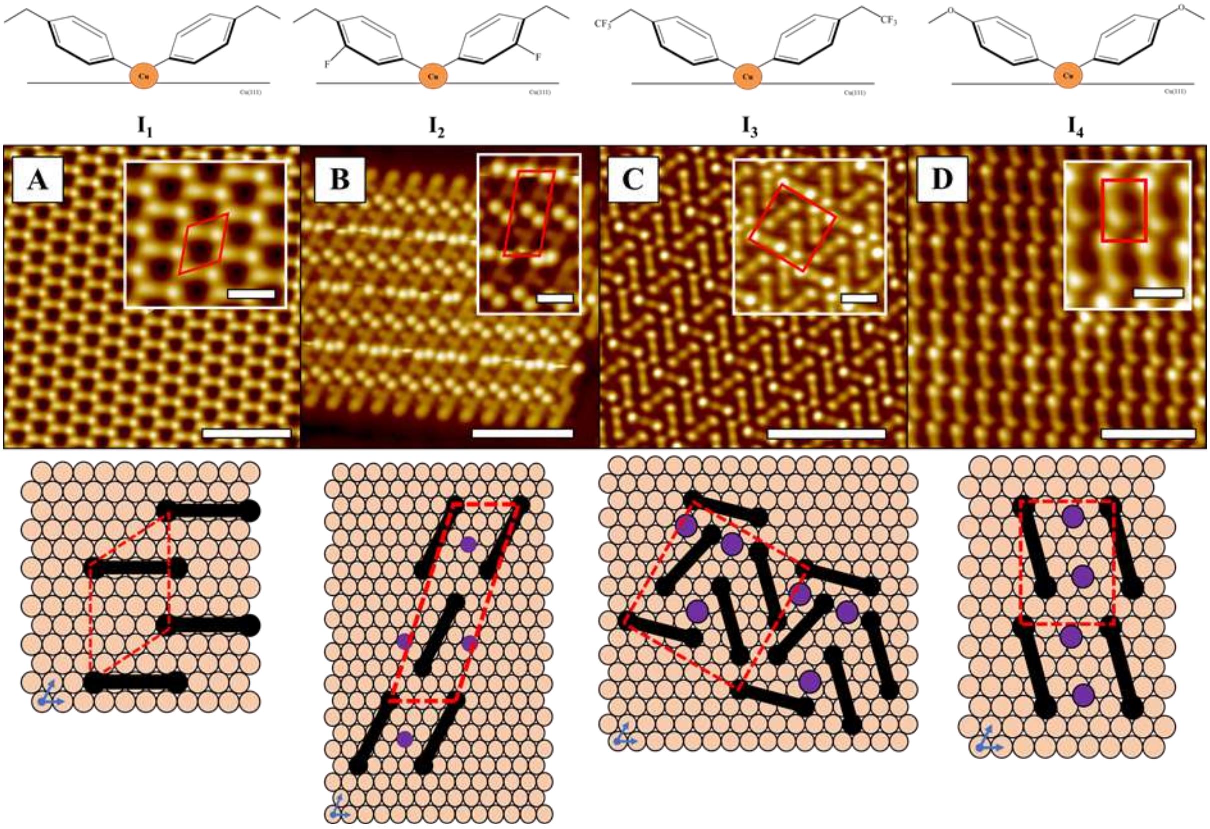

Figure 4: STM images of the four Ullmann coupling intermediate domains and their associated model schematics on Cu(111). The black molecules in the schematic are the Ullmann coupling intermediates and bromine atoms are indicated in purple. Unit cells are highlighted with red lines. **A**. **I**$_1$ on Cu(111). Inset: close-up of the domain with the unit cell overlaid in red. Below: model schematic of the unit cell of **I**$_1$ on Cu(111), its dimensions are $3\sqrt{3} \times \sqrt{19}$. **B**. **I**$_2$ on Cu(111). Inset: close-up of the domain with the unit cell overlaid in red. Below: model schematic of the unit cell **I**$_2$ on Cu(111), its dimensions are $4 \times 2\sqrt{31}$. **C**. **I**$_3$ on Cu(111). Inset: close-up of the domain with the unit cell overlaid in red. Below: model schematic of the unit cell of **I**$_3$ on Cu(111), its dimensions are $4\sqrt{3} \times 7$. **D**. **I**$_4$ on Cu(111). Inset: close-up of the domain with the unit cell overlaid in red. Below: model schematic of the unit cell of **I**$_4$ on Cu(111), its dimensions are $4 \times 3\sqrt{3}$. Scanning conditions: **A**. 200 mV, 200 pA; **B**. −10 mV, 100 pA; **C**. −50 mV, 50 pA; **D**. 200 mV, 100 pA. Scale bars: 4 nm, inset scale bars: 1 nm.

Comparing the four Ullmann coupling products, we observe that they also have very distinct domains. In **Figure 5A**, **P**$_1$ packs in an open-brick wall motif. On closer inspection the individual molecules are ordered side-by-side in pairs at the tail end of the molecules with a unit cell of $\sqrt{21} \times 4$ dimensions. In the case **P**$_2$, the precursor only differs from ethylbenzene by one fluorine atom in the *ortho* position with respect to the ethyl tail. As seen in **Figure 5B**, the arrangement of the **P**$_2$ molecules share the same open-brick wall motif as that of **P**$_1$ and they share the same unit cell dimensions. It is also noticeable that in the spaces between four **P**$_2$ molecules there are at times the circular features, bromine atoms that were cleaved from the aryl species during the copper catalyzed Ullmann reaction, which lead to slight perturbations in the spacing between molecules. Although the bromine atoms are observed in some of the spaces, it is not regular or periodic and hence is not depicted as part of the proposed **P**$_2$ unit cell.

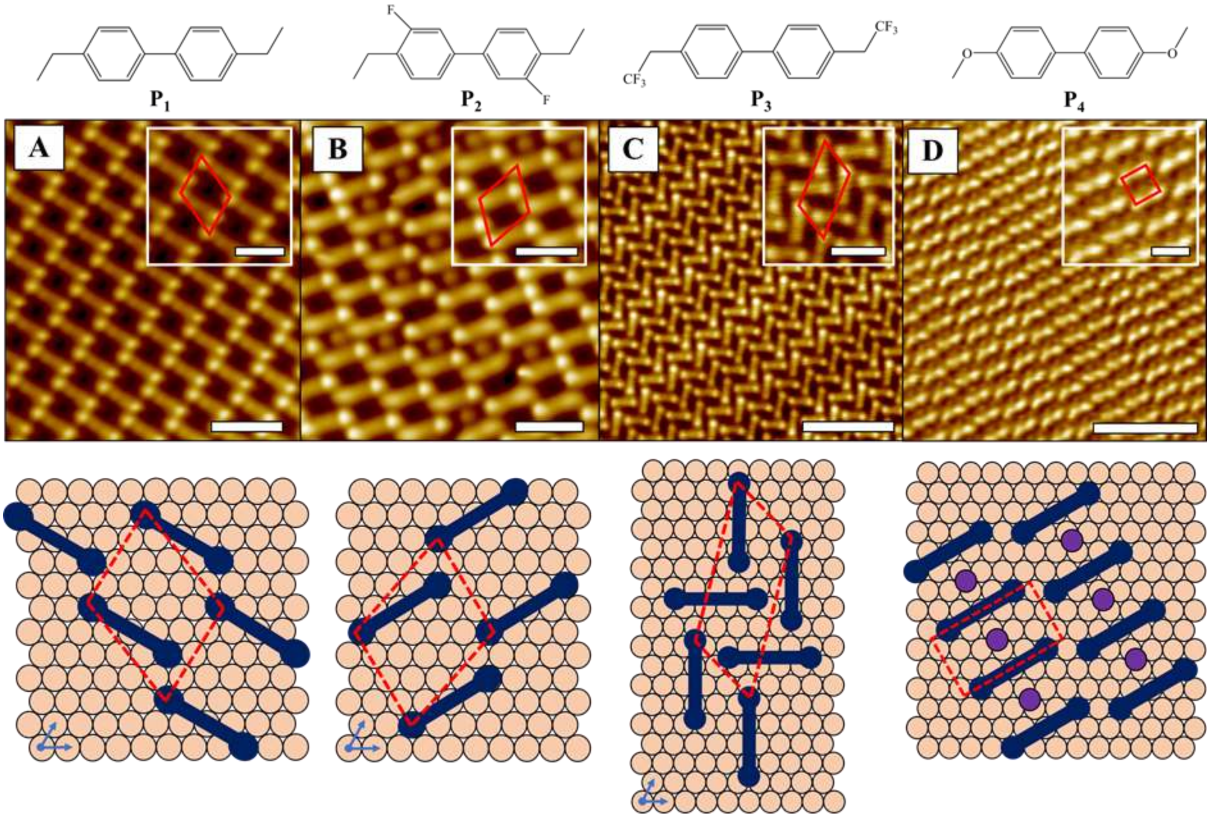

Figure 5: STM images of Ullmann coupling product domains and their associated model schematics on Cu(111). The dark blue molecules in the schematic are the Ullmann coupling domain products and bromine atoms are indicated in purple. Unit cells are highlighted with red lines. **A**. **P_1** on Cu(111). *Inset:* close-up of the domain with the unit cell overlaid in red. *Below*: model schematic of the unit cell of **P_1** on Cu(111), its dimensions are $\sqrt{21} \times 4$. **B**. **P_2** on Cu(111). *Inset*: close-up of the domain with the unit cell overlaid in red. The circular features are the dissociated Br atoms. *Below*: model schematic of the unit cell **P_2** on Cu(111), its dimensions are $4 \times \sqrt{21}$. **C**. **P_3** on Cu(111). *Inset*: close-up of the domain with the unit cell overlaid in red. *Below*: model schematic of the unit cell of **P_3** on Cu(111), its dimensions are $\sqrt{13} \times 2\sqrt{13}$. **D**. **$P_4$** on Cu(111). *Inset:* close-up of the **P_4** domain, the 1D crystal is indicated in red lines. *Below*: Model schematic of the **P_4** domains, the 1D crystal is indicated with dotted lines. Scanning conditions: **A**. −10 mV, 50 pA. Scale bar: 2 nm, inset scale bar: 1 nm; **B.** 10 mV, 100 pA. Scale bar: 2 nm, inset scale bar: 1 nm; **C**. 30 mV, 50 pA. Scale bar: 5 nm, inset scale bar: 2 nm; **D**. 200 mV, 200 pA. Scale bar: 5 nm, inset scale bar: 1 nm.

In the case of **P_3**, the ordered domains are different to **P_1** and **P_2** and have a herringbone packing structure. The unit cell has $\sqrt{13} \times 2\sqrt{13}$ dimensions. The molecules are packed close together in a manner that suggests the presence of strong electrostatic effects between the $-CH_2CF_3$ tails and the phenyl groups of adjacent molecules.[53–55] The structure of **P_4** is unique in that it does not have a true periodic crystalline structure. There is, however, a high degree of ordering in one dimension as shown in **Figure 5D**, where the 1D rows consist exclusively of just one of the surface-bound stereoisomers of the Ullmann product. Specifically, the diastereomers are *cis*, where both methoxy tails face in the same direction or *trans*, where the methoxy tails are pointed in opposing directions. As can be seen in **Figure 6B**, in which each of the unique surface-bound isomers is color coded, the 1D rows consist of just one isomer, except in areas where a defect is present. On closer inspection one sees that there is in fact cooperativity between the 1D rows in terms of the position of the methoxy tails. Specifically, every pair of adjacent molecules has their methoxy side groups pointing in opposite directions. We will return to this point later the in paper.

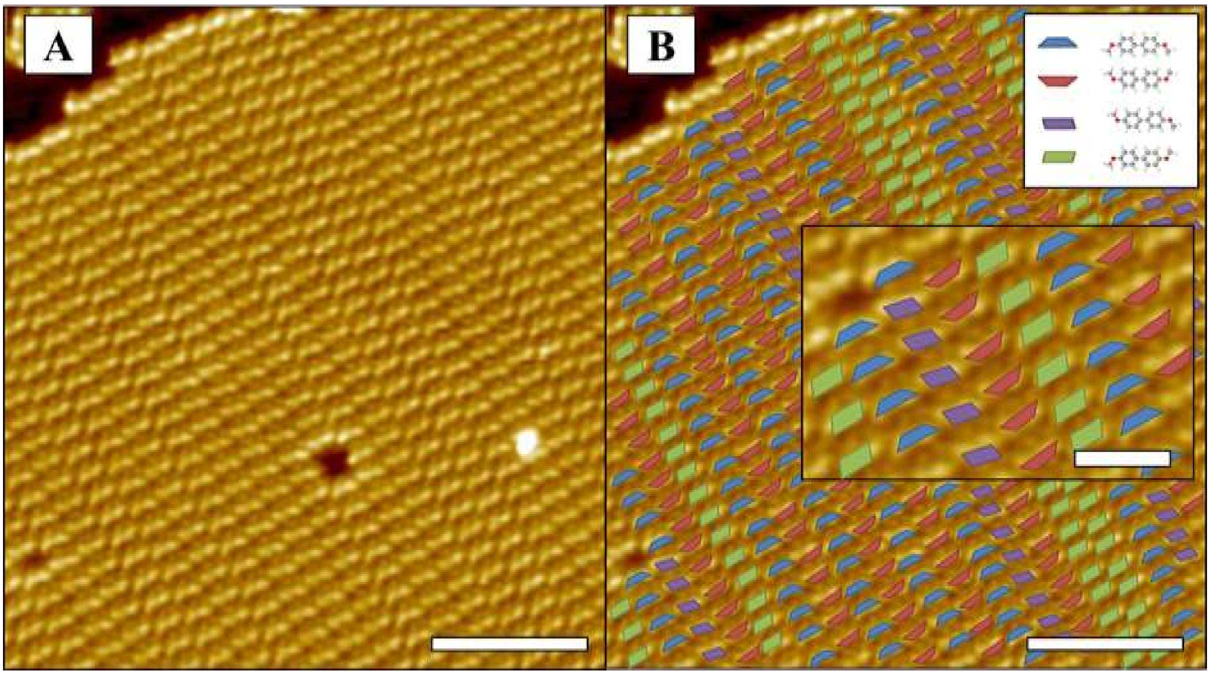

Figure 6: **A**. STM image of a domain of **P4**. **B**. STM image of the domain in A with the stereoisomers labelled with respect to the orientation of the methoxy tails. *Inset*: close-up of the rows. Scanning conditions: 200 mV, 200 pA. Scale bars: 5 nm. Inset scale bar: 2 nm.

After collecting and characterizing the ordered arrays of organometallic intermediates and products we next compared and contrasted the packing density of the arrays. Considering the size of the unit cell and the number of molecules in each unit cell we arrive at the packing density, σ, defined as the number of intermediate/product molecules per unit area as shown in **Table 2**. What is noticeable is that σ increases for the product molecules with respect to their organometallic intermediates, which is consistent with the intermediates being larger than the products due to the Cu adatom at the center of the intermediates. Interestingly, the outliers in **Table 2** (intermediate **I3** and its product **P3**) exhibit significantly higher packing density which is consistent with their highly polar $-CH_2CF_3$ tails that leads to their dense packing. In contrast, species **I1**, **I2**, **P1**, and **P2** exhibit an open brick pattern with considerably lower packing density.

Table 2: Comparison of the area of unit cells and packing density (σ) of the Ullmann coupling intermediates (**Ix**) and their respective products (**Px**). The areas and packing densities are calculated from the models shown in **Figures 4** and **5**.

Intermediate	Area of Unit Cell (nm^2)	σ (Molecules/nm^2)
I_1	1.19	0.84
I_2	2.72	0.73
I_3	3.18	1.26
I_4	1.36	0.73

Product	Area of Unit Cell (nm^2)	σ (Molecules/nm^2)
P_1	1.14	0.88
P_2	1.14	0.88
P_3	1.48	1.36
P_4	1.02	0.98

To further understand the relationship between the properties of the molecules themselves and the packing structure of the 2D domains, DFT calculations were performed for **R_1–R_4** and **P_1–P_4** (**Table S1**) and electrostatic maps were produced as well (**Figures 7** and **8**; refer to SI for more detail). Our DFT calculations confirmed that the $-CH_2CH_3$/$-CH_2CF_3$ tails of intermediates and products 1, 2 and 3 are most stable when oriented perpendicular to the phenyl ring while the methoxy tail of **I_4** and **P_4** are most stable when in plane with the phenyl ring (**Figure S1**).[43–45] In **Figure 7A**, the **I_1** species has relatively small charges and based on the orientation of the organometallic intermediates there does not seem to be a significant relationship between any local dipoles and its packing structure. However, in **Figure 7B**, the orientation of the **I_2** organometallic intermediates appear to suggest a relationship as the highly electronegative fluorine groups which are aligned with the hydrogens on the phenyl rings of adjacent intermediates. We hypothesize that this favorable electrostatic interaction leads to the lower packing density of **I_2**, relative to **I_1**.

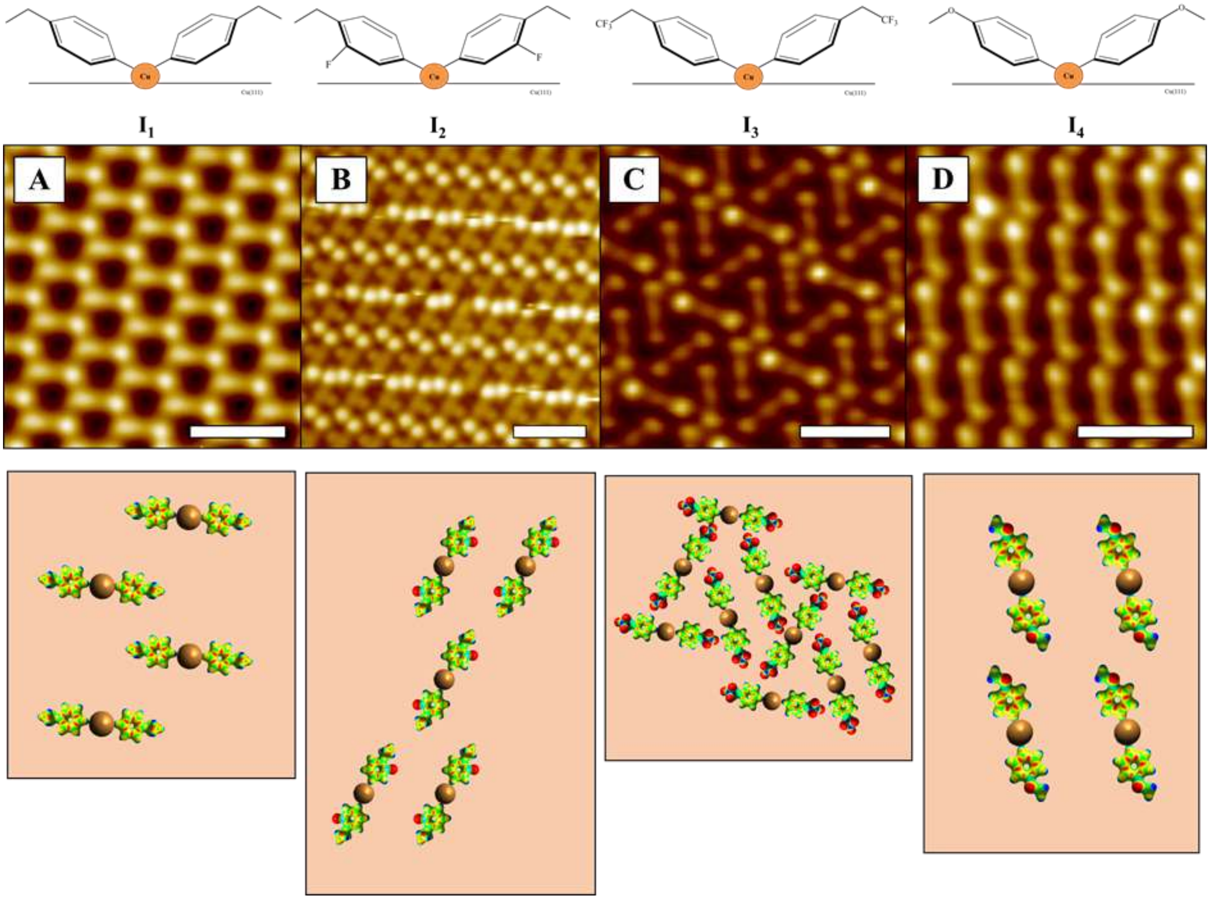

Figure 7 STM images of Ullmann coupling intermediate domains and their associated model schematics on Cu(111). The schematics are made using the DFT generated electrostatic maps for **R_1–R_4**, combined to make an intermediate molecule and then overlaid over a Cu(111) surface. **A**. **I_1** on Cu(111), its monomer has a calculated 0.3905 D dipole and $\begin{pmatrix} 2.2784 & 0.0019 & 1.6442 \\ * & 2.6310 & -0.0063 \\ * & * & -4.9093 \end{pmatrix}$ D·Å quadrupole (**Table S2**); **B**. **I_2** on Cu(111), its monomer has a calculated 1.4109 D dipole and $\begin{pmatrix} 3.9317 & 2.1130 & 1.5039 \\ * & -0.2052 & 0.9122 \\ * & * & -3.7265 \end{pmatrix}$ D·Å quadrupole (**Table S2**); **C**. **I_3** on Cu(111), its monomer has a calculated 2.6117 D dipole and $\begin{pmatrix} -1.7882 & 0.0023 & -4.3903 \\ * & 3.9368 & -0.0008 \\ * & * & -2.1486 \end{pmatrix}$ D·Å quadrupole (**Table S2**); **D**. **I_4** on Cu(111), its monomer has a calculated 1.3964 D dipole and

$\begin{pmatrix} 4.9550 & 3.1454 & 0.0000 \\ * & 0.9094 & 0.0000 \\ * & * & -5.8644 \end{pmatrix}$ D·Å quadrupole (**Table S2**). Scanning conditions: **A**. 200 mV, 200 pA; **B**. −10 mV, 100 pA; **C**. − 50 mV, 50 pA; **D**. 200 mV, 100 pA. Scale bars: 2 nm.

In **Figure 7C**, the dense packing in the **I$_3$** unit cell indicates strong electrostatic interactions between the $-CH_2CF_3$ tails and the hydrogens on the phenyl ring of the adjacent organometallic intermediate. It is presumably these electrostatic interactions that drive the very different ordering of **I$_3$** species from the open brick structure observed for the other organometallic intermediates in this study. Instead, I$_3$ has a dense tail-side packing that maximizes these interactions.

In **Figure 7D,** the relationship is very similar to that of **I$_2$** except in this case the $-OCH_3$ is the highly electronegative species. Due to this property, the orientation of the *trans* isomer is clearly explainable. The electrostatic map shows the highly electronegative oxygen in the $-OCH_3$ tail lies complimentary with the methyl moiety on the adjacent molecule's $-OCH_3$ tail. However, since the proximity of the oxygen is relatively close there is some electrostatic repulsion with the oxygen of the OCH_3 tail of the adjacent molecule. Such repulsion may also help explain the relatively low packing density within the unit cell.

When looking at the product species in **Figure 8**, we can see that the relationship between the charge distribution on the product molecules and their packing structure is clearer and many of the traits observed for the intermediates are also found for the products. Specifically, in **Figure 8A**, **P$_1$** shows the same lack of relationship between the small local charges on the molecule and its 2D domain formation. Again, a low-density open brick like packing is observed.

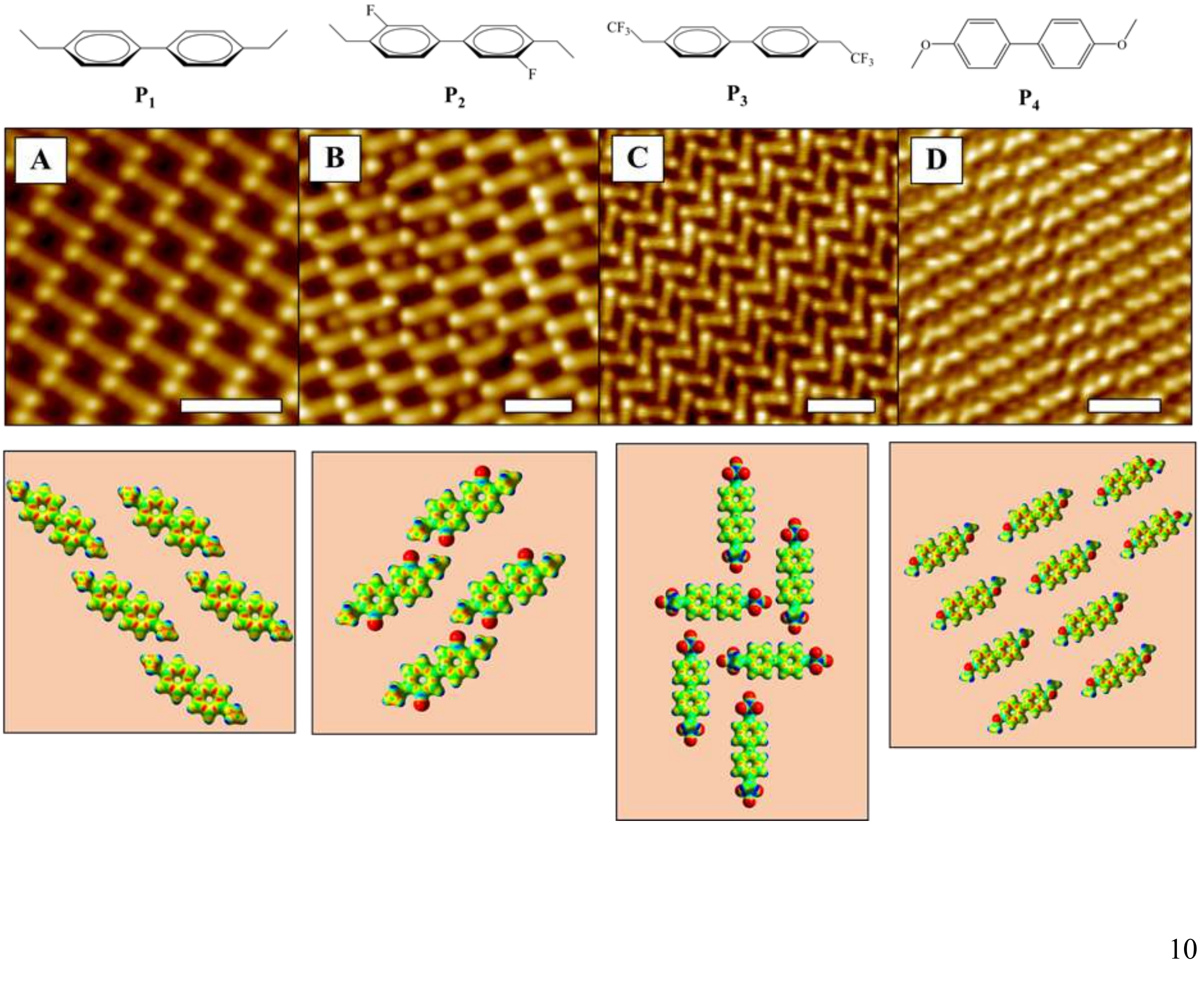

Figure 8: STM images of Ullmann coupling products and their associated model schematics on Cu(111). The schematics are made using the DFT generated electrostatic maps and then overlaid over a Cu(111) surface. **A**. $\mathbf{P_1}$ on Cu(111), configuration 2 (**Table S5**) has a calculated 0.1184 D dipole and $\begin{pmatrix} 7.9456 & 0.0003 & 0.0000 \\ * & 3.5092 & -0.0005 \\ * & * & -11.4548 \end{pmatrix}$ D·Å quadrupole; **B**. $\mathbf{P_2}$ on Cu(111), configuration 1 (**Table S5**) has a calculated 0.000 D dipole and $\begin{pmatrix} 5.1436 & -12.8970 & 1.0805 \\ * & 0.7870 & -1.5277 \\ * & * & -5.9305 \end{pmatrix}$ D·Å quadrupole; **C**. $\mathbf{P_3}$ on Cu(111), configuration 1 (**Table S5**) has a calculated 0.000 D dipole and $\begin{pmatrix} -21.4441 & 0.0383 & 22.3405 \\ * & 17.0519 & -0.0035 \\ * & * & 4.3922 \end{pmatrix}$ D·Å quadrupole; **D**. $\mathbf{P_4}$ on Cu(111), the *cis* diastereomer has a calculated 2.5576 D dipole and $\begin{pmatrix} 10.6788 & 0.0001 & 0.0001 \\ * & 2.4458 & 0.0000 \\ * & * & -13.1246 \end{pmatrix}$ D·Å quadrupole, while the *trans* diastereomer has a calculated 0.0004 D dipole and $\begin{pmatrix} 12.9502 & 14.7918 & 0.0002 \\ * & 0.4694 & 0.0000 \\ * & * & -13.4197 \end{pmatrix}$ D·Å quadrupole (**Table S5**). Scanning conditions: **A**. −10 mV, 50 pA; **B**. 10 mV, 100 pA; **C**. 30 mV, 50 pA; **D**. 200 mV, 200 pA. Scale bars: 2 nm.

In **Figure 8B**, one can see that there is a higher degree of local charging of the F atom on the phenyl ring and that the packing structure leads to favorable interactions between the F on the phenyl ring and the $-CH_2CH_3$ tail of an adjacent molecule. However, as seen in Table 2, the packing densities of $\mathbf{P_1}$ and $\mathbf{P_2}$ are the same. This may be a compensation effect whereby the larger fluorinated molecule $\mathbf{P_2}$ packs just as densely as its non-fluorinated counterpart $\mathbf{P_1}$ despite its larger size due to the fluorine atom because of the favorable interactions between the F atom on the phenyl ring and the $-CH_2CH_3$ tail of an adjacent molecule. In **Figure 8C**, it can be seen that $\mathbf{P_3}$ is an outlier in that it forms dense structures, similar to its organometallic intermediate $\mathbf{I_3}$. Specifically, for $\mathbf{P_3}$, the $-CH_2CF_3$ tails are oriented towards the hydrogens on the adjacent molecule's phenyl ring. In **Figure 8D**, the charge distribution of $\mathbf{P_4}$ matches well with the details of its packing structure as seen in **Figure 6** in that the highly electronegative oxygen of the $-OCH_3$ tail is oriented towards the methyl group of the adjacent molecule's $-OCH_3$ tail resulting in molecules in the 1D rows being all *cis* or all *trans* and also complementary stacking of the methoxy groups of adjacent molecules between the rows. Given that this complementarity between 1D rows can be achieved with either an appropriately orientated *cis* or *trans* molecule in the adjacent row, the structure does not need to be truly periodic in 2D.

5. Conclusions

By performing a comparative study of four different, but related, aryl bromides in the Cu-catalyzed Ullmann coupling reaction, and tracking the course of the reaction through its organometallic intermediate and product stages, we have been able to elucidate and understand how the structure, and specifically the charge distribution, of the molecules affects their local packing structure on the Cu(111) surface. We observe that the packing density of the intermediates is generally lower than the products because all intermediates of the Ullmann coupling reaction involve a Cu atom that elongates their structures. With the exception of the highly polar $\mathbf{I_3}$ and $\mathbf{P_3}$ species, all intermediates and products pack in an open brick like structure. For the case of $\mathbf{I_2}$/$\mathbf{I_4}$ and $\mathbf{P_2}$/$\mathbf{P_4}$, the open brick structure enables favorable electrostatic interactions between polar parts of the molecules. The highly polar $\mathbf{I_3}$ and $\mathbf{P_3}$ species pack in their own unique structures that enable favorable electrostatic interactions and are more densely packed than the others. Interestingly, for the case of $\mathbf{P_4}$, the molecules arrange in 1D rows of just one of the four different surface-bound isomers (*cis*/*trans*) of the product, but there is no long range 2D ordering of these 1D rows. However, interaction of the polar methoxy tails of the **P**$_4$ molecules in adjacent rows is complementarity, which leads to short adjacent row–row ordering but not long-range ordering. Together, these data demonstrate that highly ordered arrays of both organometallic intermediates and products are formed on the Cu surface during the Ullmann coupling reaction and that their structures and packing densities can be understood by considering the charge distribution on the molecules themselves.

6. Supporting Information Available:

See Supporting Information for details of the theoretical calculations for the dipole and electrostatic maps of the Ullmann Coupling precursors, intermediates and products. This material is available free of charge via the Internet at http://pubs.acs.org.

7. Acknowledgments

The authors thank the U.S. National Science Foundation (Grant CHE-1764270) for support of the project.

8. References

(1) Ullmann, F.; Bielecki, J. Ueber Synthesen in Der Biphenylreihe. *Berichte der Dtsch. Chem. Gesellschaft* **1901**, *34* (2), 2174–2185.

(2) Monnier, F.; Taillefer, M. Catalytic C-C, C-N, and C-O Ullmann-Type Coupling Reactions. *Angew. Chemie Int. Ed.* **2009**, *48* (38), 6954–6971.

(3) Barton, D.; Gao, H. Y.; Held, P. A.; Studer, A.; Fuchs, H.; Doltsinis, N. L.; Neugebauer, J. Formation of Organometallic Intermediate States in On-Surface Ullmann Couplings. *Chem. - A Eur. J.* **2017**, *23* (25), 6190–6197.

(4) Abe, H.; Nagai, T.; Imai, H.; Horino, Y. Improved Synthesis of Nigricanin. *Chem. Pharm. Bull. (Tokyo).* **2017**, *65* (11), 1078–1080.

(5) Fanta, P. E. The Ullmann Synthesis of Biaryls. *Chem. Rev.* **1946**, *38* (1), 139–196.

(6) Fanta, P. E. The Ullmann Synthesis of Biaryls. *Synthesis (Stuttg).* **1974**, *1974* (01), 9–21.

(7) Fuson, R. C.; Cleveland, E. A. 2,2’-Dinitrobiphenyl [Biphenyl, 2,2’-Dinitro-]. *Org. Synth.* **1940**, *20*, 45.

(8) Lo, Q. A.; Sale, D.; Braddock, D. C.; Davies, R. P. Mechanistic and Performance Studies on the Ligand-Promoted Ullmann Amination Reaction. *ACS Catal.* **2018**, *8* (1), 101–109.

(9) Mullick, K.; Biswas, S.; Kim, C.; Ramprasad, R.; Angeles-Boza, A. M.; Suib, S. L. Ullmann Reaction Catalyzed by Heterogeneous Mesoporous Copper/Manganese Oxide: A Kinetic and Mechanistic Analysis. *Inorg. Chem.* **2017**, *56* (17), 10290–10297.

(10) Zhou, F.; Guo, J.; Liu, J.; Ding, K.; Yu, S.; Cai, Q. Copper-Catalyzed Desymmetric Intramolecular Ullmann C–N Coupling: An Enantioselective Preparation of Indolines. *J. Am. Chem. Soc.* **2012**, *134* (35), 14326–14329.

(11) Hamdouchi, C.; de Blas, J.; Ezquerra, J. A Novel Application of the Ullmann Coupling Reaction for the Alkylsulfenylation of 2-Amino-Imidazo[1,2-a]Pyridine. *Tetrahedron* **1999**, *55* (2), 541–548.

(12) Surry, D. S.; Buchwald, S. L. Diamine Ligands in Copper-Catalyzed Reactions. *Chem. Sci.* **2010**, *1* (1), 13.

(13) Fischer, C.; Koenig, B. Palladium- and Copper-Mediated N -Aryl Bond Formation Reactions for the Synthesis of Biological Active Compounds. *Beilstein J. Org. Chem.* **2011**, *7* (Ii), 59–74.

(14) Buck, E.; Song, Z. J. Preparation of 1-Methoxy-2-(4-Methoxyphenoxy)Benzene. *Org. Synth.* **2005**, *82*, 69.

(15) Gao, A.; Zhang, H.; Hu, L.; Hou, A.; Xie, K. Fabrication of Silica Nanoparticle-Supported Copper Quantum Dots and the Efficient Catalytic Ullmann Coupling Reaction. *Catal. Commun.* **2017**, *102* (July), 118–122.

(16) Giri, R.; Brusoe, A.; Troshin, K.; Wang, J. Y.; Font, M.; Hartwig, J. F. Mechanism of the Ullmann Biaryl Ether Synthesis Catalyzed by Complexes of Anionic Ligands: Evidence for the Reaction of Iodoarenes with Ligated Anionic CuI Intermediates. *J. Am. Chem. Soc.* **2018**, *140* (2), 793–806.

(17) Chen, X.-Y.; Li, Z.-H.; Liu, J.-Q.; Wang, X.-S. Copper-Catalyzed Synthesis of Dibenzo[b,f]Imidazo[1,2-d][1,4]Oxazepine Derivatives via a Double Ullmann Coupling Reaction. *Synthesis (Stuttg).* **2019**, *51* (07), 1662–1668.

(18) Gong, X.; Wu, J.; Meng, Y.; Zhang, Y.; Ye, L.-W.; Zhu, C. Ligand-Free Palladium Catalyzed Ullmann Biaryl Synthesis: 'Household' Reagents and Mild Reaction Conditions. *Green Chem.* **2019**, *21* (5), 995–999.

(19) Moorthy, M.; Kannan, B.; Madheswaran, B.; Rangappan, R. Tethering of Cu(II) Schiff Base Metal Complex on Mesoporous Material MCM-41: Catalyst for Ullmann-Type Coupling Reactions. *J. Porous Mater.* **2016**, *23* (4), 977–986.

(20) Ma, D.; Cai, Q. N, N-Dimethyl Glycine-Promoted Ullmann Coupling Reaction of Phenols and Aryl Halides. *Org. Lett.* **2003**, *5* (21), 3799–3802.

(21) Lei, A.; Liu, W.; Liu, C.; Chen, M. Arylation of Unactivated Arenes. *Dalt. Trans.* **2010**, *39* (43), 10352.

(22) Baqi, Y.; Müller, C. E. Rapid and Efficient Microwave-Assisted Copper(0)-Catalyzed Ullmann Coupling Reaction: General Access to Anilinoanthraquinone Derivatives. *Org. Lett.* **2007**, *9* (7), 1271–1274.

(23) Hassan, J.; Sévignon, M.; Gozzi, C.; Schulz, E.; Lemaire, M. Aryl−Aryl Bond Formation One Century after the Discovery of the Ullmann Reaction. *Chem. Rev.* **2002**, *102* (5), 1359–1470.

(24) Sperotto, E.; van Klink, G. P. M.; van Koten, G.; de Vries, J. G. The Mechanism of the Modified Ullmann Reaction. *Dalt. Trans.* **2010**, *39* (43), 10338.

(25) Mondal, S. Recent Advancement of Ullmann-Type Coupling Reactions in the Formation of C–C Bond. *ChemTexts* **2016**, *2* (4), 17.

(26) Cai, Q.; Zhou, W. Ullmann-Ma Reaction: Development, Scope and Applications in

Organic Synthesis. *Chinese J. Chem.* **2020**, *38* (8), 879–893.

(27) Ma, D.; Cai, Q. Copper/Amino Acid Catalyzed Cross-Couplings of Aryl and Vinyl Halides with Nucleophiles. *Acc. Chem. Res.* **2008**, *41* (11), 1450–1460.

(28) Ribas, X.; Güell, I. Cu(I)/Cu(III) Catalytic Cycle Involved in Ullmann-Type Cross-Coupling Reactions. *Pure Appl. Chem.* **2014**, *86* (3), 345–360.

(29) Xi, M.; Bent, B. E. Iodobenzene on Cu(111): Formation and Coupling of Adsorbed Phenyl Groups. *Surf. Sci.* **1992**, *278* (1–2), 19–32.

(30) Wang, W.; Shi, X.; Wang, S.; Van Hove, M. A.; Lin, N. Single-Molecule Resolution of an Organometallic Intermediate in a Surface-Supported Ullmann Coupling Reaction. *J. Am. Chem. Soc.* **2011**, *133* (34), 13264–13267.

(31) Fan, Q.; Zhu, J.; Gottfried, J. M. On-Surface Ullmann Reaction for the Synthesis of Polymers and Macrocycles. In *On-Surface Synthesis II*; de Oteyza, D. G., Rogero, C., Eds.; Springer International Publishing: Cham, 2018; pp 83–112.

(32) Xi, M.; Bent, B. E. Mechanisms of the Ullmann Coupling Reaction in Adsorbed Monolayers. *J. Am. Chem. Soc.* **1993**, *115* (16), 7426–7433.

(33) Eichhorn, J.; Nieckarz, D.; Ochs, O.; Samanta, D.; Schmittel, M.; Szabelski, P. J.; Lackinger, M. On-Surface Ullmann Coupling: The Influence of Kinetic Reaction Parameters on the Morphology and Quality of Covalent Networks. *ACS Nano* **2014**, *8* (8), 7880–7889.

(34) Clair, S.; de Oteyza, D. G. Controlling a Chemical Coupling Reaction on a Surface: Tools and Strategies for On-Surface Synthesis. *Chem. Rev.* **2019**, *119* (7), 4717–4776.

(35) Zint, S.; Ebeling, D.; Schlöder, T.; Ahles, S.; Mollenhauer, D.; Wegner, H. A.; Schirmeisen, A. Imaging Successive Intermediate States of the On-Surface Ullmann Reaction on Cu(111): Role of the Metal Coordination. *ACS Nano* **2017**, *11* (4), 4183–4190.

(36) Shi, K. J.; Yuan, D. W.; Wang, C. X.; Shu, C. H.; Li, D. Y.; Shi, Z. L.; Wu, X. Y.; Liu, P. N. Ullmann Reaction of Aryl Chlorides on Various Surfaces and the Application in Stepwise Growth of 2D Covalent Organic Frameworks. *Org. Lett.* **2016**, *18* (6), 1282–1285.

(37) Lewis, E. A.; Marcinkowski, M. D.; Murphy, C. J.; Liriano, M. L.; Therrien, A. J.; Pronschinske, A.; Sykes, E. C. H. H. Controlling Selectivity in the Ullmann Reaction on Cu(111). *Chem. Commun.* **2017**, *53* (55), 7816–7819.

(38) Yang, M. X.; Xi, M.; Yuan, H.; Bent, B. E.; Stevens, P.; White, J. M. NEXAFS Studies of Halobenzenes and Phenyl Groups on Cu(111). *Surf. Sci.* **1995**, *341* (1–2), 9–18.

(39) Blake, M. M.; Nanayakkara, S. U.; Claridge, S. A.; Fernández-Torres, L. C.; Sykes, E. C. H.; Weiss, P. S. Identifying Reactive Intermediates in the Ullmann Coupling Reaction by Scanning Tunneling Microscopy and Spectroscopy. *J. Phys. Chem. A* **2009**, *113* (47), 13167–13172.

(40) McCarty, G. S.; Weiss, P. S. Footprints of a Surface Chemical Reaction: Dissociative Chemisorption of p -Diiodobenzene on Cu{111}. *J. Phys. Chem. B* **2002**, *106* (33), 8005–8008.

(41) McCarty, G. S.; Weiss, P. S. Formation and Manipulation of Protopolymer Chains. *J. Am. Chem. Soc.* **2004**, *126* (51), 16772–16776.

(42) Lackinger, M. Surface-Assisted Ullmann Coupling. *Chem. Commun.* **2017**, *53* (56), 7872–7885.

(43) Balema, T. A.; Ulumuddin, N.; Murphy, C. J.; Slough, D. P.; Smith, Z. C.; Hannagan, R. T.; Wasio, N. A.; Larson, A. M.; Patel, D. A.; Groden, K.; McEwen, J.-S.; Lin, Y.-S.; Sykes, E. C. H. Controlling Molecular Switching via Chemical Functionality: Ethyl vs Methoxy Rotors. *J. Phys. Chem. C* **2019**, *123* (38), 23738–23746.

(44) Wasio, N. A.; Slough, D. P.; Smith, Z. C.; Ivimey, C. J.; Thomas III, S. W.; Lin, Y.-S.; Sykes, E. C. H. Correlated Rotational Switching in Two-Dimensional Self-Assembled Molecular Rotor Arrays. *Nat. Commun.* **2017**, *8* (1), 16057.

(45) Murphy, C. J.; Smith, Z. C.; Pronschinski, A.; Lewis, E. A.; Liriano, M. L.; Wong, C.; Ivimey, C. J.; Duffy, M.; Musial, W.; J. Therrien, A.; Thomas III, S. W.; Sykes, E. C. H. Ullmann Coupling Mediated Assembly of an Electrically Driven Altitudinal Molecular Rotor. *Phys. Chem. Chem. Phys.* **2015**, *17* (47), 31931–31937.

(46) Hla, S.-W.; Bartels, L.; Meyer, G.; Rieder, K.-H. Inducing All Steps of a Chemical Reaction with the Scanning Tunneling Microscope Tip: Towards Single Molecule Engineering. *Phys. Rev. Lett.* **2000**, *85* (13), 2777–2780.

(47) Rastgoo Lahrood, A.; Björk, J.; Heckl, W. M.; Lackinger, M. 1,3-Diiodobenzene on Cu(111) – an Exceptional Case of on-Surface Ullmann Coupling. *Chem. Commun.* **2015**, *51* (68), 13301–13304.

(48) Basagni, A.; Ferrighi, L.; Cattelan, M.; Nicolas, L.; Handrup, K.; Vaghi, L.; Papagni, A.; Sedona, F.; Valentin, C. Di; Agnoli, S.; Sambi, M. On-Surface Photo-Dissociation of C–Br Bonds: Towards Room Temperature Ullmann Coupling. *Chem. Commun.* **2015**, *51* (63), 12593–12596.

(49) Sambiagio, C.; Marsden, S. P.; Blacker, A. J.; McGowan, P. C. Copper Catalysed Ullmann Type Chemistry: From Mechanistic Aspects to Modern Development. *Chem. Soc. Rev.* **2014**, *43* (10), 3525–3550.

(50) Nguyen, M. T.; Pignedoli, C. A.; Passerone, D. An Ab Initio Insight into the Cu(111)-Mediated Ullmann Reaction. *Phys. Chem. Chem. Phys.* **2011**, *13* (1), 154–160.

(51) Frisch, M. J.; Trucks, G. W.; Schlegel, H. B.; Scuseria, G. E.; Robb, M. A.; Cheeseman, J. R.; Scalmani, G.; Barone, V.; Mennucci, B.; Petersson, G. A.; Nakatsuji, H.; Caricato, M.; Li, X.; Hratchian, H. P.; Izmaylov, A. F.; Bloino, J.; Zheng, G.; Sonnenb, D. J. Gaussian 09, Revision D.01. Gaussian, Inc.: Wallingford, CT 2013.

(52) Singh, U. C.; Kollman, P. A. An Approach to Computing Electrostatic Charges for Molecules. *J. Comput. Chem.* **1984**, *5* (2), 129–145.

(53) Meyers, J. M.; Gellman, A. J. The Investigation of Fluorinated Propenes on the Cu(111) Surface. *Surf. Sci.* **1995**, *339* (1–2), 57–67.

(54) Wong, K. L.; Lin, X.; Kwon, K.-Y.; Pawin, G.; Rao, B. V.; Liu, A.; Bartels, L.; Stolbov, S.; Rahman, T. S. Halogen-Substituted Thiophenol Molecules on Cu(111). *Langmuir* **2004**, *20* (25), 10928–10934.

(55) Wong, K.; Kwon, K. Y.; Rao, B. V.; Liu, A.; Bartels, L. Effect of Halo Substitution on the Geometry of Arenethiol Films on Cu(111). *J. Am. Chem. Soc.* **2004**, *126* (25), 7762–7763.

TOC Image